Title

Imaging stress and magnetism at high pressures using a nanoscale quantum sensor.

Journal

Science (New York, N.Y.), 366(6471)

ISSN

0036-8075

Authors

Hsieh, S
Bhattacharyya, P
Zu, C
et al.

Publication Date

2019-12-01

DOI

10.1126/science.aaw4352

Peer reviewed

HIGH-PRESSURE PHYSICS

Imaging stress and magnetism at high pressures using a nanoscale quantum sensor

S. Hsieh[1,2]*, P. Bhattacharyya[1,2]*, C. Zu[1]*, T. Mittiga[1], T. J. Smart[3], F. Machado[1], B. Kobrin[1,2], T. O. Höhn[1,4], N. Z. Rui[1], M. Kamrani[5], S. Chatterjee[1], S. Choi[1], M. Zaletel[1], V. V. Struzhkin[6], J. E. Moore[1,2], V. I. Levitas[5,7,8], R. Jeanloz[3], N. Y. Yao[1,2]†

Pressure alters the physical, chemical, and electronic properties of matter. The diamond anvil cell enables tabletop experiments to investigate a diverse landscape of high-pressure phenomena. Here, we introduce and use a nanoscale sensing platform that integrates nitrogen-vacancy (NV) color centers directly into the culet of diamond anvils. We demonstrate the versatility of this platform by performing diffraction-limited imaging of both stress fields and magnetism as a function of pressure and temperature. We quantify all normal and shear stress components and demonstrate vector magnetic field imaging, enabling measurement of the pressure-driven $\alpha \leftrightarrow \epsilon$ phase transition in iron and the complex pressure-temperature phase diagram of gadolinium. A complementary NV-sensing modality using noise spectroscopy enables the characterization of phase transitions even in the absence of static magnetic signatures.

In hybrid quantum-sensing devices, sensors are directly integrated into existing toolsets ranging from biological imaging to materials spectroscopy (*1*–*4*). Here, we demonstrate the versatility of a platform based on quantum spin defects combined with static high-pressure technologies (*5*, *6*). In particular, we instrument diamond anvil cells (DACs) with a layer of nitrogen-vacancy (NV) centers directly at the culet, enabling the pursuit of two complementary objectives in high-pressure science: understanding the strength and failure of materials under pressure (e.g., the brittle-ductile transition) and discovering and characterizing exotic phases of matter (e.g., pressure-stabilized high-temperature superconductors) (*7*–*11*). Achieving these goals hinges upon the sensitive in situ imaging of signals within the high-pressure chamber. For the first goal, measuring the local stress environment permits the direct observation of inhomogeneities in plastic flow and the formation of line defects. For the second goal, the ability to spatially resolve field distributions can provide a direct image of complex order parameters and textured phenomena such as magnetic domains. However, the enormous stress gradients generated near the sample limit the utility of most conventional tabletop spectroscopy techniques; as a result, one is often restricted to measuring bulk properties averaged over the entire DAC geometry.

Our approach to these challenges is to use an ensemble of NV centers [~1 part per million (ppm) density] implanted ~50 nm from the surface of the diamond anvil culet (Fig. 1, A and B). Each NV center represents an atomic-scale defect (i.e., a substitutional nitrogen impurity adjacent to a vacancy) inside the diamond lattice and exhibits an $S = 1$ electronic spin ground state (*12*). In the absence of external fields, the $|m_s = \pm 1\rangle$ spin sublevels are degenerate and separated by $D_{gs} = (2\pi) \times 2.87$ GHz from the $|m_s = 0\rangle$ state. Crucially, both the nature and energy of these spin states are sensitive to local changes in stress, temperature, and magnetic and electric fields (Fig. 1C) (*13*–*19*). These spin states can be optically initialized and read out, as well as coherently manipulated through microwave fields. Their energy levels can be probed by performing optically detected magnetic resonance (ODMR) spectroscopy, which measures a change in the NV's fluorescence intensity when an applied microwave field is on resonance between two NV spin sublevels (Fig. 1D), thus enabling a variety of external signals to be sensed over a wide range of environmental conditions (*1*, *20*, *21*).

Here, we focus on the sensing of stress and magnetic fields, wherein the NV is governed by the Hamiltonian (*18*, *22*), $H = H_0 + H_B + H_S$, with $H_0 = D_{gs} S_z^2$ (zero-field splitting), $H_B = \gamma_B \vec{B} \cdot \vec{S}$ (Zeeman splitting), and $H_S = [\alpha_1(\sigma_{xx} + \sigma_{yy}) + \beta_1 \sigma_{zz}] S_z^2 + [\alpha_2(\sigma_{yy} - \sigma_{xx}) + \beta_2(2\sigma_{xz})](S_y^2 - S_x^2) + [\alpha_2(2\sigma_{xy}) + \beta_2(2\sigma_{yz})](S_x S_y + S_y S_x)$ capturing the NV's response to the local diamond stress tensor, $\overleftrightarrow{\sigma}$ (Fig. 1C). In the above, $\gamma_B \approx (2\pi) \times 2.8$ MHz/G is the gyromagnetic ratio, $\{\alpha_{1,2}, \beta_{1,2}\}$ are the stress susceptibility coefficients (*17*–*19*, *23*), $\hat{z}$ is the NV orientation axis, and $\hat{x}$ is defined such that the xz plane contains one of the carbon-vacancy bonds (Fig. 1E). In general, the resulting ODMR spectra exhibit eight resonances arising from the four possible crystallographic orientations of the NV (Fig. 1D). By extracting the energy shifting and splitting of the spin sublevels for each NV orientation group, one obtains an overconstrained set of equations enabling the reconstruction of either the (six component) local stress tensor or the (three component) vector magnetic field (*23*).

In our experiments, we use a miniature DAC (Fig. 1, A and B) consisting of two opposing anvils compressing either a beryllium copper or rhenium gasket (*24*). The sample chamber defined by the gasket and diamond-anvil culets is filled with a pressure-transmitting medium (either a 16:3:1 methanol/ethanol/water solution or cesium iodide) to provide a quasi-hydrostatic environment. Microwave excitation is applied with a 4-μm-thick platinum foil compressed between the gasket and anvil pavilion facets (fig. S1); scanning confocal microscopy (with a transverse diffraction-limited spot size of ~600 nm, containing ~10^3 NVs) allows us to obtain two-dimensional ODMR maps across the culet.

We begin by probing the stress tensor across the culet surface (up to $P = 48$ GPa as shown in fig. S7) using two different cuts of diamond [i.e., (111)-cut and (110)-cut culet]. For a generic stress environment, the intrinsic degeneracy associated with the four NV orientations is not sufficiently lifted, implying that individual resonances cannot be resolved. To resolve these resonances while preserving the stress contribution, we sequentially tune a precisely controlled external magnetic field to be perpendicular to each of the different NV orientations (*23*). For each perpendicular field choice, three of the four NV orientations exhibit a strong Zeeman splitting proportional to the projection of the external magnetic field along their symmetry axes. Notably, this enables one to resolve the stress information encoded in the remaining NV orientation, whereas the other three groups of NVs are spectroscopically split away. Using this method, we obtain sufficient information to extract the full stress tensor, as depicted in Fig. 2. A number of intriguing features are observed at the interface between the culet and the sample chamber, which provide insight into both elastic (reversible) and plastic (irreversible) deformations.

At low pressures ($P = 4.9$ GPa), the normal stress along the loading axis, σ_{ZZ}, is spatially uniform (Fig. 2A), whereas all shear stresses, $\{\sigma_{XY}, \sigma_{XZ}, \sigma_{YZ}\}$, are minimal (Fig. 2B). The axes $\{\hat{X}, \hat{Y}, \hat{Z}\}$ correspond to the lab frame, whereas $\{\hat{x}, \hat{y}, \hat{z}\}$ correspond to the NV frame (Fig. 1, A and E). These observations are in agreement with conventional stress continuity predictions for the interface between a solid and an ideal fluid (*25*). Moreover, σ_{ZZ} is consistent with the independently measured pressure inside the sample chamber (by ruby fluorescence),

[1]Department of Physics, University of California, Berkeley, CA 94720, USA. [2]Materials Science Division, Lawrence Berkeley National Laboratory, Berkeley, CA 94720, USA. [3]Department of Earth and Planetary Science, University of California, Berkeley, CA 94720, USA. [4]Fakultät für Physik, Ludwig-Maximilians-Universität München, 80799 Munich, Germany. [5]Department of Aerospace Engineering, Iowa State University, Ames, IA 50011, USA. [6]Geophysical Laboratory, Carnegie Institution of Washington, Washington, DC 20015, USA. [7]Department of Mechanical Engineering, Iowa State University, Ames, IA 50011, USA. [8]Ames Laboratory, Division of Materials Science and Engineering, Ames, IA 50011, USA.
*These authors contributed equally to this work.
†Corresponding author. Email: norman.yao@berkeley.edu

demonstrating the NV's potential as a built-in pressure scale (*26*). In contrast to the uniformity of σ_{ZZ}, the field profile for the mean lateral stress, $\sigma_{\perp} \equiv \frac{1}{2}(\sigma_{XX} + \sigma_{YY})$, exhibits a concentration of forces toward the center of the culet (Fig. 2A). Using the measured σ_{ZZ} as a boundary condition, we perform finite-element simulations to reproduce this spatial pattern (*23*).

Upon increasing pressure ($P = 13.6$ GPa), a spatial gradient in σ_{ZZ} emerges (Fig. 2B, inset). This qualitatively distinct feature is consistent with the solidification of the pressure-transmitting medium into its glassy phase above $P_g \approx 10.5$ GPa (*27*). Crucially, this demonstrates our ability to characterize the effective viscosity of solids and liquids under pressure. To characterize the sensitivity of our system, we perform ODMR spectroscopy with a static applied magnetic field and pressure under varying integration times and extract the frequency uncertainty from a Gaussian fit. We observe a stress sensitivity of $\{0.023, 0.030, 0.027\}$ GPa/$\sqrt{\text{Hz}}$ for hydrostatic, average normal, and average shear stresses, respectively. This is consistent with the theoretically derived stress sensitivity, $\eta_S \sim \frac{\Delta\nu}{\xi C\sqrt{Nt}} = \{0.017, 0.022, 0.020\}$ GPa/$\sqrt{\text{Hz}}$, where N is the number of NV centers, $\Delta\nu$ is the linewidth, ξ is the relevant stress susceptibility, t is the integration time, and C is an overall factor accounting for measurement infidelity (*23*). In combination with diffraction-limited imaging resolution, this sensitivity makes it possible to measure and ultimately control the full stress tensor distribution across a sample.

Having characterized the stress environment, we use the NV centers as an in situ magnetometer to detect phase transitions inside the high-pressure chamber. Analogous to the case of stress, we observe a magnetic sensitivity of 12 μT/$\sqrt{\text{Hz}}$, in agreement with the theoretically estimated value, $\eta_B \sim \frac{\delta\nu}{C\gamma_B B\sqrt{Nt}} = 8.8$ μT/$\sqrt{\text{Hz}}$. Assuming a point dipole located a distance $d \sim 5$ μm from the NV layer, this corresponds to an experimentally measured magnetic moment sensitivity: 7.5×10^{-12} emu/$\sqrt{\text{Hz}}$ (Fig. 1F).

After determining the sensitivity, we begin by directly measuring the magnetization of iron as it undergoes the pressure-driven $\alpha \leftrightarrow \epsilon$ phase transition from body-centered cubic (bcc) to hexagonal close-packed (hcp) crystal structures (*28*); crucially, this structural phase transition is accompanied by the depletion of the magnetic moment, and it is this change in the iron's magnetic behavior that we image. The sample chamber is loaded with a ~10-μm polycrystalline iron pellet as well as a ruby microsphere (pressure scale), and we apply an external magnetic field B_{ext}~180 G. As before, by performing a confocal scan across the culet, we acquire a two-dimensional magnetic resonance map (Fig. 3). At low pressures (Fig. 3A), near the iron pellet, we observe substantial shifts in the eight NV resonances, owing to the presence of a ferromagnetic field from the iron pellet. As one increases pressure (Fig. 3B), these shifts begin to diminish, signaling a reduction in the magnetic susceptibility. Finally, at the highest pressures ($P \sim$ 22 GPa, Fig. 3C), the magnetic field from the

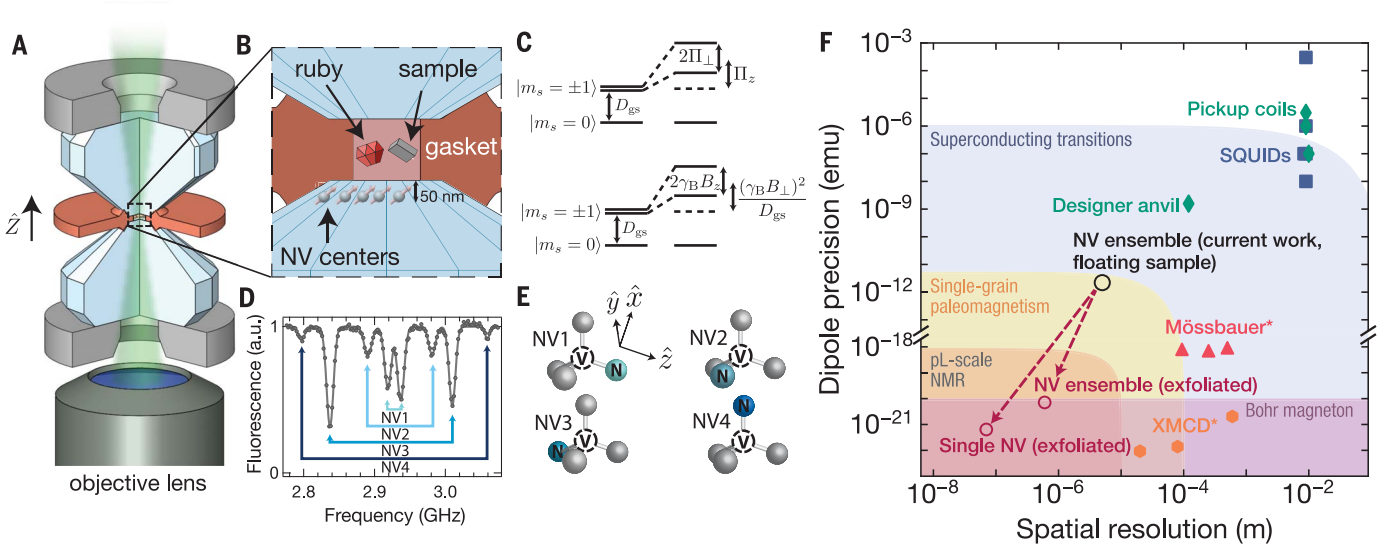

Fig. 1. NV centers integrated into a diamond anvil cell. (**A**) Schematic of the DAC geometry. Two opposing anvils are compressed by a nonmagnetic steel cell and cubic boron nitride backing plates (gray). NV centers are initialized and read out using a 532-nm laser focused to a diffraction-limited spot (~600 nm), which is scanned across the culet surface. (**B**) The DAC sample chamber is defined by the gasket-anvil assembly (diagram not to scale); it is loaded with the sample of interest, a pressure-transmitting medium, and a single ruby microsphere (pressure calibration). A ~50-nm layer of NV centers is embedded into the diamond anvil directly below the sample chamber. (**C**) Top: Stress both shifts and splits the $m_s = \pm 1$ sublevels at first order; in particular, the shifting is characterized by $\Pi_z = \alpha_1(\sigma_{xx} + \sigma_{yy}) + \beta_1\sigma_{zz}$, and the splitting is characterized by $\Pi_\perp^2 = [\alpha_2(\sigma_{yy} - \sigma_{xx}) + \beta_2(2\sigma_{xz})]^2 + [\alpha_2(2\sigma_{xy}) + \beta_2(2\sigma_{yz})]^2$. Bottom: An axial magnetic field splits the $m_s = \pm 1$ sublevels at first order, but a transverse magnetic field leads to shifts only at second order. (**D**) A representative ODMR spectrum from an NV center ensemble under an applied magnetic field. (**E**) Each pair of resonances in (D) corresponds to one of the four NV crystallographic orientations. (**F**) Comparison of high-pressure magnetometry techniques. We define the spatial resolution as a characteristic sensor length scale over which the sample magnetism is integrated. Estimates for our current work are shown assuming a sample suspended in a pressure medium 5 μm away from the culet (black open circle). We project that by exfoliating a sample directly onto the culet surface and using 5-nm implanted NV centers, the distance from the sample can be substantially reduced, thus improving both dipole precision and spatial resolution (open red circles). Inductive methods [pickup coils (green diamonds) and superconducting quantum interference devices (SQUIDs) (blue squares)] integrate the magnetization of a sample over the coil's area (*23*); to this end, the diameter associated with the coil is taken as the "spatial resolution" although in principle, the sample inside the chamber can be substantially smaller. By contrast, high-energy photon scattering techniques [x-ray magnetic circular dichroism (orange hexagons), and Mössbauer spectroscopy (pink triangles)] probe atomic-scale magnetism (*23*); the length scale for these methods is shown here as the spot size of the excitation beam.

pellet has decreased by more than two orders of magnitude.

To quantify this phase transition, we reconstruct the full vector magnetic field produced by the iron sample from the aforementioned two-dimensional NV magnetic resonance maps (Fig. 3, D to F). We then compare this information with the expected field distribution at the NV layer inside the culet, assuming the iron pellet generates a dipole field (*23*). This enables us to extract an effective dipole moment as a function of applied pressure (Fig. 3G). To identify the critical pressure, we fit the transition using a logistic function (*23*). This procedure yields the transition at $P = 16.7 \pm 0.7$ GPa (Fig. 3J).

In addition to changes in the magnetic behavior, another key signature of this first-order transition is the presence of hysteresis. We investigate this by slowly decompressing the diamond anvil cell and monitoring the dipole moment; the decompression transition occurs at $P = 10.5 \pm 0.7$ GPa (Fig. 3J), suggesting a hysteresis width of ~6 GPa, consistent with a combination of intrinsic hysteresis and finite shear stresses in the methanol/ethanol/water pressure-transmitting medium (*28*). Taking the average of the forward and backward hysteresis pressures, we find a critical pressure of $P_c = 13.6 \pm 3.6$ GPa, in excellent agreement with independent measurements by Mössbauer spectroscopy, where $P_c \approx 12$ GPa (Fig. 3J) (*28*).

Next, we demonstrate the integration of our platform into a cryogenic system, enabling us to make spatially resolved in situ measurements across the pressure-temperature (*P-T*) phase diagram of materials. Specifically, we investigate the magnetic *P-T* phase diagram of the rare-earth element gadolinium (Gd) up to pressures $P \approx 8$ GPa and between temperatures $T = 25$ to 340 K. Owing to an interplay between localized 4f electrons and mobile conduction electrons, Gd represents an interesting playground for studying metallic magnetism; in particular, the itinerant electrons mediate RKKY-type interactions between the local moments, which in turn induce spin-polarization of the itinerant electrons (*29*). Moreover, much like its rare-earth cousins, Gd exhibits a series of pressure-driven structural phase transitions from hcp to samarium-type (Sm-type) to double hcp (dhcp) (Fig. 4) (*30*). The interplay between these different structural phases, various types of magnetic ordering, and metastable transition dynamics leads to a complex magnetic *P-T* phase diagram that remains the object of study to this day (*29*–*31*).

In analogy to our measurements of iron, we monitor the magnetic ordering of a Gd flake by using the NV's ODMR spectra at two different locations inside the culet: close to and far away from the sample (the latter to be used as a control) (fig. S15). Because of thermal contraction of the DAC (which induces a change in pressure), each experimental run traces a distinct non-isobaric path through the *P-T* phase diagram (Fig. 4C, blue curves). In addition to these DC magnetometry measurements, we also operate the NV sensors in a complementary mode, i.e., as a noise spectrometer.

We begin by characterizing Gd's well-known ferromagnetic Curie transition at ambient pressure, which induces a sharp jump in the splitting of the NV resonances at $T_C = 292.2 \pm 0.1$ K (Fig. 4D). As depicted in Fig. 4A, upon increasing pressure, this transition shifts to lower temperatures, and consonant with its second-order nature (*32*), we observe no hysteresis (Fig. 4A, inset); this motivates us to fit the data and extract T_C by solving a regularized Landau free-energy equation (*23*). Combining all of the low-pressure data (Fig. 4C, red squares), we find a linear decrease in the Curie temperature at a rate $dT_C/dP = -18.7 \pm 0.2$ K/GPa, consistent with prior studies using both DC conductivity and AC-magnetic susceptibility (*30*). Unexpectedly, this linear decrease extends well into the Sm-type phase. Upon increasing pressure above ~6 GPa (path [b] in Fig. 4C), we observe the loss of ferromagnetic (FM) signal (Fig. 4B), indicating a first-order structural transition into the paramagnetic (PM) dhcp phase (*30*). In stark contrast to the previous Curie transition, there is no revival of a ferromagnetic signal even after heating up (~315 K) and substantially reducing the pressure (to < 0.1 GPa).

A few remarks are in order. The linear decrease of T_C well beyond the ~2-GPa structural transition between hcp- and Sm-type is consistent with the "sluggish" equilibration

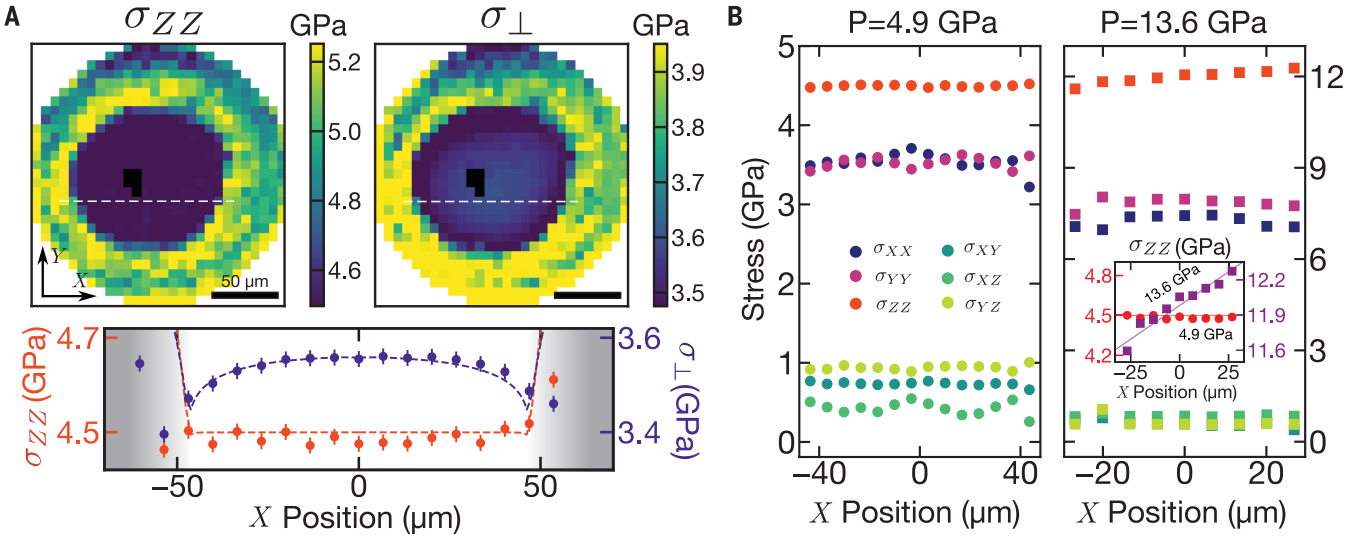

Fig. 2. Full tensorial reconstruction of the stresses in a (111)-cut diamond anvil. (**A**) Spatially resolved maps of the loading stress (left) and mean lateral stress (right), $\sigma_\perp = \frac{1}{2}(\sigma_{XX} + \sigma_{YY})$, across the culet surface. In the inner region, where the culet surface contacts the pressure-transmitting medium (16:3:1 methanol/ethanol/water), the loading stress is spatially uniform, whereas the lateral stress is concentrated toward the center; this qualitative difference is highlighted by a linecut (taken along the white-dashed line) of the two stresses (below), and reconstructed by finite-element analysis (orange and purple dashed lines). The black pixels indicate where the NV spectrum was obfuscated by the ruby microsphere. (**B**) Comparison of all stress tensor components in the fluid-contact region at $P = 4.9$ GPa and $P = 13.6$ GPa. At $P = 13.6$ GPa, the pressure-transmitting medium has entered its glassy phase, and we observe a spatial gradient in the loading stress σ_{ZZ} (inset).

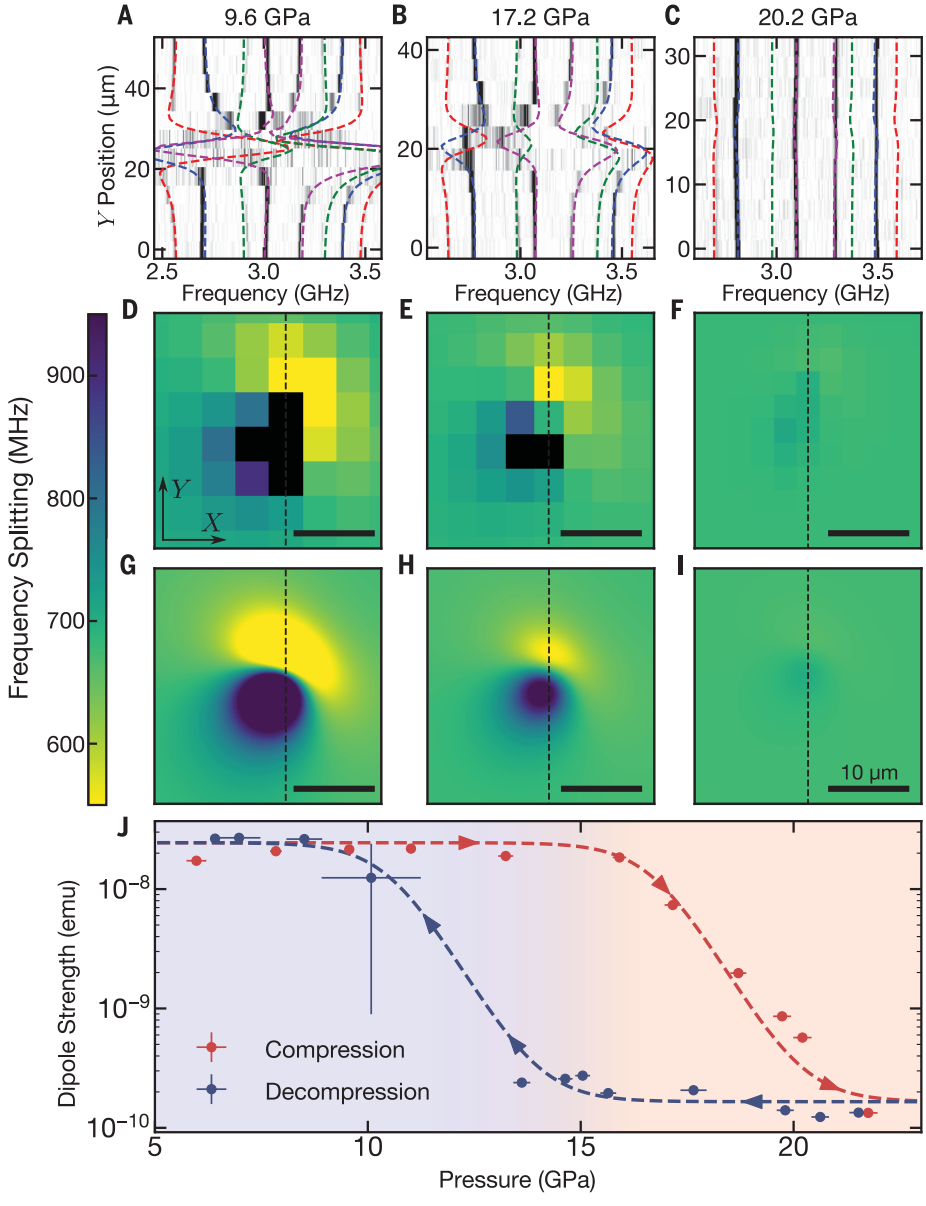

Fig. 3. Imaging iron's $\alpha \leftrightarrow \epsilon$ phase transition. Applying an external magnetic field ($B_{ext} \sim 180$ G) induces a dipole moment in the polycrystalline iron pellet that generates a spatially varying magnetic field across the culet of the diamond anvil. By mapping the ODMR spectra across the culet surface, we reconstruct the local magnetic field that characterizes the iron pellet's magnetization. (**A** to **C**) Comparison between the measured ODMR spectra (dark regions correspond to resonances) and the theoretical resonance positions (different colors correspond to different NV crystallographic orientations) across vertical spatial cuts (i.e., *Y* position indicates location along the black-dashed line shown in the two-dimensional scans below) at pressures of 9.6, 17.2, and 20.2 GPa, respectively (16:3:1 methanol/ethanol/water solution). (**D** to **F**) Map of the measured energy difference of a particular NV crystallographic orientation [blue lines in (A) to (C)]. Black pixels correspond to ODMR spectra where the splitting could not be accurately extracted owing to large magnetic field gradients (fig. S12). (**G** to **I**) Theoretical reconstruction of the energy differences shown in (D) to (F) (*23*). Data depicted in (A) to (C) are taken along the thin black dashed lines. (**J**) Measured dipole moment of the iron pellet as a function of applied pressure at room temperature, for both compression (red) and decompression (blue). Based on the hysteresis observed (~6 GPa), we find the critical pressure $P_c = 13.6 \pm 3.6$ GPa, in excellent agreement with previous studies (*28*).

between these two phases at low temperatures (*30*). The metastable dynamics of this transition are strongly pressure and temperature dependent, suggesting that different starting points (in the *P-T* phase diagram) can exhibit markedly different behaviors (*30*). To highlight this, we probe two different transitions out of the paramagnetic Sm-type phase by tailoring specific paths in the *P-T* phase diagram. By taking a shallow path in *P-T* space, we observe a small change in the local magnetic field across the structural transition into the PM dhcp phase at ~6 GPa (Fig. 4C, path [c], orange diamonds). By taking a steeper path in *P-T* space, one can also investigate the magnetic transition into the antiferromagnetic (AFM) Sm-type phase at ~150 K (Fig. 4C, path [d], green triangle). In general, these two transitions are extremely challenging to probe via DC magnetometry because their signals arise only from small differences in the susceptibilities between the various phases (fig. S18).

To this end, we demonstrate a complementary NV sensing modality based on noise spectroscopy, which can probe phase transitions even in the absence of a direct magnetic signal (*33*). Specifically, returning to Gd's ferromagnetic Curie transition, we monitor the NV's depolarization time, T_1, as the phase transition is crossed (Fig. 4D). Normally, the NV's T_1 time is limited by spin-phonon interactions and increases sharply as the temperature is decreased. Here, we observe a markedly disparate behavior. In particular, using nanodiamonds drop-cast on a Gd foil at ambient pressure, we find that the NV T_1 is nearly temperature independent in the paramagnetic phase, before exhibiting a kink and subsequent decrease upon entering the ferromagnetic phase (Fig. 4D). We note two intriguing observations: first, one possible microscopic explanation for this behavior is that T_1 is dominated by Johnson-Nyquist noise from the thermal fluctuations of charge carriers inside Gd (*34*, *35*). Gapless critical spin fluctuations or magnons in the ordered phase, although expected, are less likely to cause this signal (*23*). Second, we observe that the Curie temperature, as identified by T_1-noise spectroscopy, is ~10 K higher than that observed via DC magnetometry (Fig. 4D). Similar behavior has previously been reported for the surface of Gd (*29*, *36*), suggesting that our noise spectroscopy could be more sensitive to surface physics.

Further stress characterization of other fluids and solids may provide insights into

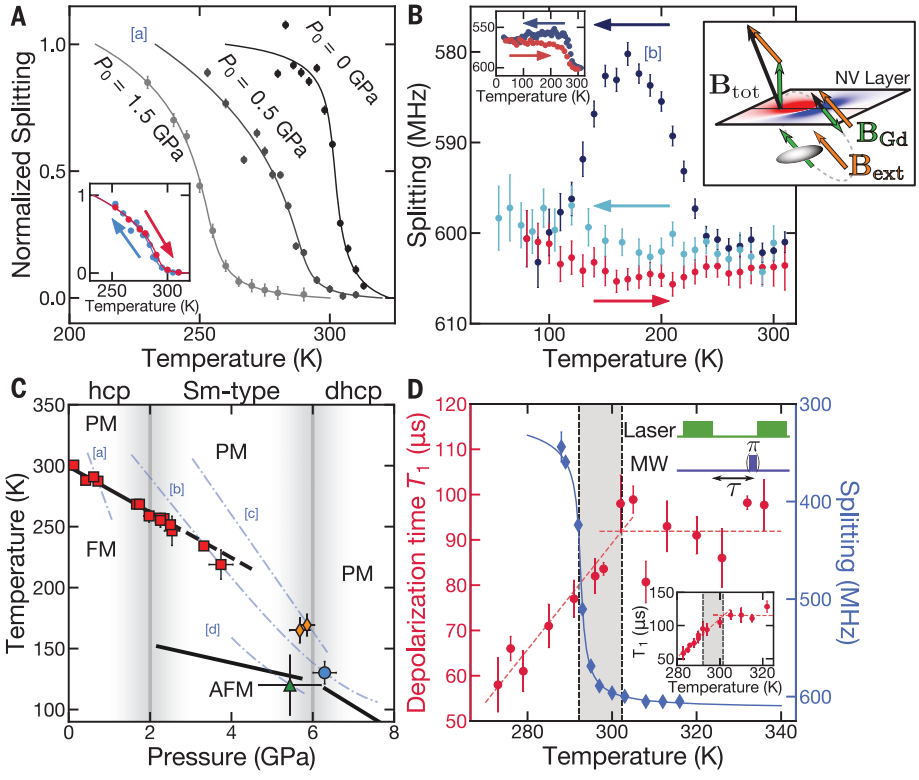

Fig. 4. Magnetic P-T phase diagram of gadolinium. A ~ 30 μm by 30 μm by 25 μm polycrystalline Gd foil is loaded into a beryllium copper gasket with a cesium iodide pressure medium. An external magnetic field, B_{ext} ~ 120 G, induces a dipole field, B_{Gd}, detected by the splitting of the NVs [right inset, (B)]. (**A**) The FM Curie temperature T_C decreases with increasing pressure up to ~4 GPa. NV splittings for three *P-T* paths, labeled by their initial pressure P_0, are shown. The *P-T* path for run [a] (P_0 = 0.5 GPa) is shown in (C). The cool-down (blue) and heat-up (red) of a single *P-T* cycle shows negligible hysteresis (inset). (**B**) If a *P-T* path starting in hcp is taken into the dhcp phase (at pressures ≳6 GPa) (*30*), the FM signal is lost and not reversible, as shown in (C) (path [b]). Upon cool-down (dark blue), we observe the aforementioned Curie transition, followed by the loss of FM signal at 6.3 GPa, 130 K. But upon heat-up (red) and second cool-down (light blue), the FM signal is not recovered. When the pressure does not go beyond ~6 GPa, the FM signal is recoverable (left inset) (*23*). (**C**) Magnetic *P-T* phase diagram of Gd. At low pressures, we observe the linear decrease of T_C (black line) with slope −18.7 ± 0.2 K/GPa, in agreement with previous measurements (*30*). This linear regime extends into the Sm-type phase (black dashed line) owing to the slow dynamics of the hcp → Sm-type transition (*30*). When starting in the Sm-type phase, we no longer observe a FM signal, but rather a small change in the magnetic field at either the transition from Sm-type to dhcp (orange diamonds) or from PM to AFM (green triangle), depending on the *P-T* path. The bottom two phase boundaries (black lines) are taken from (*31*). (**D**) At ambient pressure, we observe a Curie temperature, T_C = 292.2 ± 0.1 K, by using DC magnetometry (blue data). Using nanodiamonds drop-cast onto a Gd foil (and no applied external magnetic field), we find that the depolarization time (T_1) of the NVs is qualitatively different in the two phases (red data). T_1 is measured using the pulse sequence shown in the top right inset. The T_1 measurement on another nanodiamond exhibits nearly identical behavior (bottom inset).

mechanical phenomena such as viscous flow, plastic deformation, and pressure-dependent yield strength. Such information is challenging to obtain by either numerical finite-element simulations or more conventional experimental methods and may ultimately allow control of the deviatoric- as well as normal-stress conditions in high-pressure experiments (*37*).

The high sensitivity and close proximity of our sensor enables the measurement of signals in settings that are beyond the capabilities of existing techniques (Fig. 1F). Such settings include, for example, nuclear magnetic resonance (NMR) at picoliter volumes (*38*) and single-grain remnant magnetism (*39*), as well as phenomena that exhibit spatial textures such as magnetic skyrmions (*4*) and superconducting vortices (*40*).

Although our work uses NV centers, the techniques developed here can be readily extended to other atomic defects. For instance, recent developments on all-optical control of silicon-vacancy centers in diamond may allow for microwave-free stress imaging with improved sensitivities (*41*). In addition, one can consider defects in other anvil substrates beyond diamond; indeed, recent studies have shown that moissanite (6H silicon carbide) hosts optically active defects that show promise as local sensors (*41*). In contrast to millimeter-scale diamond anvils, moissanite anvils can be manufactured at centimeter or larger scales, and therefore support larger sample volumes that ameliorate the technical requirements of many experiments. Finally, the suite of sensing capabilities previously demonstrated for NV centers (i.e., electric, thermal, gyroscopic precession, etc.) can now straightforwardly be extended to high-pressure environments, opening up a large range of experiments for quantitatively characterizing materials at such extreme conditions.

REFERENCES AND NOTES

1. G. Kucsko *et al.*, *Nature* **500**, 54–58 (2013).
2. P. Maletinsky *et al.*, *Nat. Nanotechnol.* **7**, 320–324 (2012).
3. J. Cai, F. Jelezko, M. B. Plenio, *Nat. Commun.* **5**, 4065 (2014).
4. Y. Dovzhenko *et al.*, *Nat. Commun.* **9**, 2712 (2018).
5. A. Jayaraman, *Rev. Mod. Phys.* **55**, 65–108 (1983).
6. H. Mao, X.-J. Chen, Y. Ding, B. Li, L. Wang, *Rev. Mod. Phys.* **90**, 015007 (2018).
7. E. Wigner, H. Huntington, *J. Chem. Phys.* **3**, 764–770 (1935).
8. H. Horii, S. Nemat-Nasser, *Philos. Trans. A Math. Phys. Eng. Sci.* **319**, 337–374 (1986).
9. E. Gilioli, L. Ehm, *IUCrJ* **1**, 590–603 (2014).
10. A. P. Drozdov, M. I. Eremets, I. A. Troyan, V. Ksenofontov, S. I. Shylin, *Nature* **525**, 73–76 (2015).
11. M. Somayazulu *et al.*, *Phys. Rev. Lett.* **122**, 027001 (2019).
12. M. W. Doherty *et al.*, *Phys. Rep.* **528**, 1–45 (2013).
13. V. M. Acosta *et al.*, *Phys. Rev. Lett.* **104**, 070801 (2010).
14. J. R. Maze *et al.*, *Nature* **455**, 644–647 (2008).
15. F. Dolde *et al.*, *Nat. Phys.* **7**, 459–463 (2011).
16. P. Ovartchaiyapong, K. W. Lee, B. A. Myers, A. C. B. Jayich, *Nat. Commun.* **5**, 4429 (2014).
17. M. W. Doherty *et al.*, *Phys. Rev. Lett.* **112**, 047601 (2014).
18. M. S. J. Barson *et al.*, *Nano Lett.* **17**, 1496–1503 (2017).
19. L. G. Steele *et al.*, *Appl. Phys. Lett.* **111**, 221903 (2017).
20. F. Casola, T. van der Sar, A. Yacoby, *Nat. Rev. Mater.* **3**, 17088 (2018) Review Article.
21. T. Mittiga *et al.*, *Phys. Rev. Lett.* **121**, 246402 (2018).
22. P. Udvarhelyi, V. O. Shkolnikov, A. Gali, G. Burkard, A. Pályi, *Phys. Rev. B* **98**, 075201 (2018).
23. See supplementary materials for additional details.
24. E. Sterer, M. P. Pasternak, R. D. Taylor, *Rev. Sci. Instrum.* **61**, 1117–1119 (1990).
25. G. Falkovich, *Fluid Mechanics* (Cambridge Univ. Press, ed. 2, 2018).
26. A. Dewaele, P. Loubeyre, M. Mezouar, *Phys. Rev. B Condens. Matter Mater. Phys.* **70**, 094112 (2004).
27. S. Klotz, J.-C. Chervin, P. Munsch, G. Le Marchand, *J. Phys. D Appl. Phys.* **42**, 075413 (2009).
28. R. Taylor, M. Pasternak, R. Jeanloz, *J. Appl. Phys.* **69**, 6126–6128 (1991).
29. L. Oroszlány, A. Deák, E. Simon, S. Khmelevskyi, L. Szunyogh, *Phys. Rev. Lett.* **115**, 096402 (2015).
30. A. Jayaraman, in *Metals* , vol. 1 of *Handbook on the Physics and Chemistry of Rare Earths* (Elsevier, 1978), pp. 707–747.
31. G. K. Samudrala, G. M. Tsoi, S. T. Weir, Y. K. Vohra, *High Press. Res.* **34**, 385–391 (2014).

32. P. Hargraves, R. A. Dunlap, D. J. W. Geldart, S. P. Ritcey, *Phys. Rev. B Condens. Matter* **38**, 2862–2864 (1988).
33. S. Chatterjee, J. F. Rodriguez-Nieva, E. Demler, *Phys. Rev. B* **99**, 104425 (2019).
34. S. Kolkowitz *et al*., *Science* **347**, 1129–1132 (2015).
35. As opposed to isolated NV samples, where T_1 is limited by spin-phonon interactions.
36. H. Tang *et al*., *Phys. Rev. Lett.* **71**, 444–447 (1993).
37. B. Feng, V. I. Levitas, R. J. Hemley, *Int. J. Plast.* **84**, 33–57 (2016).
38. P. Kehayias *et al*., *Nat. Commun.* **8**, 188 (2017).
39. D. R. Glenn *et al*., *Geochem. Geophys. Geosyst.* **18**, 3254–3267 (2017).
40. L. Thiel *et al*., *Nat. Nanotechnol.* **11**, 677–681 (2016).
41. M. Atatüre, D. Englund, N. Vamivakas, S.-Y. Lee, J. Wrachtrup, *Nat. Rev. Mater.* **3**, 38–51 (2018).
42. S. Hsieh *et al*., Imaging stress and magnetism at high pressures using a nanoscale quantum sensor, Zenodo (2019); doi.org/10.5281/zenodo.3334404.

ACKNOWLEDGMENTS

We gratefully acknowledge fruitful discussions with J. Analytis, R. Birgeneau, J. Choi, K. de Greve, M. Eremets, Z. Geballe, F. Hellman, A. Jarmola, J. Jeffries, I. Kim, M. Kunz, D.-H. Lee, S. Lewin, P. Maurer, R. Ramesh, G. Samudrala, E. Zepeda-Alarcon, and R. Zieve. We thank D. Budker, P. Fischer, and H. Zhou for a careful reading of the manuscript and helpful comments. We are especially grateful to M. Barson and M. Doherty for sharing their raw data on stress susceptibilities. We thank C. Laumann for introducing us to the idea of integrating NV centers into diamond anvil cells. **Funding:** This work was supported as part of the Center for Novel Pathways to Quantum Coherence in Materials, an Energy Frontier Research Center funded by the U.S. Department of Energy, Office of Science, Basic Energy Sciences under Award no. DE-AC02-05CH11231. N.Y.Y. acknowledges support from the David and Lucile Packard foundation and the W. M. Keck foundation. S.H. acknowledges support from the National Science Foundation Graduate Research Fellowship under grant no. DGE-1752814. T.J.S. and R.J. acknowledge support from the U.S. Department of Energy National Nuclear Security Administration under grant no. DE-NA0003842. V.I.L. and M.K. acknowledge support from the Army Research Office (grant W911NF-17-1-0225) and the National Science Foundation (grants CMMI-1536925 and DMR-1904830). **Author contributions:** S.H., P.B., C.Z., T.M., T.J.S., and T.O.H. performed the experiments and collected data. F.M., B.K., N.Z.R., S. Chatterjee, S. Choi, M.Z., J.E.M., and N.Y.Y. developed theoretical models and methodology. S.H, P.B., C.Z., T.M., T.O.H., F.M., B.K., and S. Chatterjee performed the data analysis. M.K. and V.I.L. performed the finite-element simulations. V.V.S. provided equipment and technical expertise for the diamond anvil cells. N.Y.Y. and R.J. conceived the study and supervised the project. All authors contributed to discussions of the data and to the writing of the manuscript. **Competing interests:** University of California (coinventors S.H., P.B., C.Z., T.M., T.J.S., F.M., B.K., S.C., J.E.M., R.J., and N.Y.Y.) filed for a provisional patent (62/782,262) that relates to sensing at high pressures using an apparatus that integrates defects in diamond with diamond anvil cells. **Data and materials availability:** Published data are available on the Zenodo public database (*42*).

SUPPLEMENTARY MATERIALS

science.sciencemag.org/content/366/[6471/1349/suppl/DC1
Supplementary Text
Figs. S1 to S21
Tables S1 and S2
References (*43*–*70*)

21 December 2018; accepted 6 November 2019
10.1126/science.aaw4352

Imaging stress and magnetism at high pressures using a nanoscale quantum sensor

S. Hsieh, P. Bhattacharyya, C. Zu, T. Mittiga, T. J. Smart, F. Machado, B. Kobrin, T. O. Höhn, N. Z. Rui, M. Kamrani, S. Chatterjee, S. Choi, M. Zaletel, V. V. Struzhkin, J. E. Moore, V. I. Levitas, R. Jeanloz and N. Y. Yao

Science **366** (6471), 1349-1354.
DOI: 10.1126/science.aaw4352

Diamond-based sensors

Material properties can change dramatically under pressure. Typically, to achieve high-pressure conditions, researchers place their samples in diamond anvil cells (DACs). However, monitoring the properties of the sample inside a DAC is tricky (see the Perspective by Hamlin and Zhou). Hsieh *et al.*, Lesik *et al.*, and Yip *et al.* developed monitoring techniques based on nitrogen-vacancy (NV) centers in diamond. The NV centers can act as sensors because their energy levels and the associated spectra are sensitive to strain and magnetic fields. This enabled optical readout of a spatially resolved signal.

Science, this issue p. 1349, p. 1359, p. 1355; see also p. 1312